IMPROVEMENT OF AIR TEMPERATURE AND FLOW FIELDS IN FLAT STEEL COOLING BEDS BASED ON CFD SIMULATIONS

by

Anda REN[a], Tingrong HUANG[a], Qinglu SONG[a], Sai ZHOU[a], Zhanjie LIU[b], and Dechang WANG[a*]

[a] College of Mechanical and Electrical Engineering, Qingdao University, Qingdao, China
[b] Haier Biomedical Co. Ltd., High-Tech Zone, Qingdao, China

Original scientific paper
https://doi.org/10.2298/TSCI250711205R

During the cooling process of the flat steel under the insulation cover, the cold air-flowing in from the gaps of the cooling bed has an excessive flow rate, causing the cooling speed of the flat steel at this location be too fast. This results in an uneven cooling rate of the flat steel, making it prone to bending and having an excessively high hardness, which reduces the product quality of the flat steel. Therefore, the chimney effect ducts and mechanical ventilation structure were proposed to reduce the air velocity at the gaps of the cooling bed and improve the uniformity of the temperature field of the flat steel. The air temperature field and flow field of the cooling bed were simulated using the ANSYS FLUENT software. Based on the simulation results, the effects of three chimney effect structures and a mechanical exhaust device on the air-flow velocity at the gap and on the temperature distribution of the flat steel were analyzed. According to the research results, it is found that the air velocity at the gap of the cooling bed directly affects the temperature difference, ΔT, between the flat steel at the gap and non-gap locations, and the larger the air velocity, the larger the ΔT. The four proposed improvement schemes can effectively reduce the air velocity at the gap and decrease ΔT, among which the small pipe hot air structure based on the chimney effect performs the best, which can reduce the air velocity at the gap by 73.8% and ΔT by 47.73%. In addition, this structure can utilize the waste heat to form a natural chimney effect, which has significant advantages in terms of energy saving and environmental protection.

Introduction

Flat steel is widely used in the manufacturing of machines, equipment, tools and automotive parts, *etc*. The production process of flat steel involves multiple steps. Among them, during the heating and cooling processes, the flat steel is cooled on the cooling bed under the effect of the insulation cover at the prescribed cooling rate. The cooling bed is used to correct the deformation and ensure uniform cooling of each part, thereby guaranteeing the dimensional accuracy. However, since the gear used for the moving flat steel is a moving part, the cooling bed adopts a segmented structure. The defect of this structure often leads to the excessive cooling speed of the flat steel at the gaps between each segment, resulting in uneven cooling of the entire flat steel and causing bending due to cooling and excessive hardness in some areas, thereby reducing the quality of the product. Therefore, the cooling stage is critical for improving overall product quality [1].

* Corresponding author, e-mail: wdechang@163.com

The study shows that the bending of flat steel is the result of the combined effects of temperature gradients, phase transformation strain, and mechanical stress. An *et al*. [2] used a numerical model to reveal the 3-D deformation patterns of strip material during rolling, while Qiu *et al*. [3] established a finite element model that confirmed the coupled effect of temperature and phase transformation during the cooling stage can cause a sudden increase in the bending of the strip steel. Li *et al*. [4] found that the three-fold bending of *L*-shaped steel stems from the interaction between phase transformation strain and cooling contraction strain. Chen *et al*. [5] pointed out that differences in cooling rates of rails lead to asynchronous temperature and phase transformation, and proposed the *pre-bending method* to improve the flatness of rails after cooling. Pernia *et al.* [6] used CFD-FEM coupled simulation optimize the cooling bed structure, improving cooling uniformity by adding heat reflection plates and reducing beam spacing, thereby reducing bending by 9%. Ren *et al*. [7] controlled the holding time and flipping mode of the ingot, reducing the bending of square ingots by 2.5%. Kong *et al*. [8] adjusted the cooling bed operating speed and the temperature of the slow-cooling pit to effectively avoid bending in flat steel. Cai and Song [9] improved the straightness of steel by regulating the cooling bed operating rate.

The aforementioned studies show that the thermal-mechanical-phase transition coupling effect caused by temperature gradients is the key mechanism behind the bending of flat steel. Temperature gradients, as the driving force behind solid stress and deformation, also induce the chimney effect in fluid dynamics and are widely used in the construction industry. Although steel cooling and construction belong to different fields, they are fundamentally based on the principles of heat transfer and fluid dynamics. To reduce the local cooling rate of flat steel, the heat released can be utilized to induce the chimney effect, drawing cold air from below the gaps in the cooling bed, reducing air-flow at the gaps, improving temperature uniformity, and minimizing flat steel bending.

To successfully apply this method to flat steel cooling, it is crucial to thoroughly understand the dynamics and heat transfer characteristics of buoyancy-driven air-flow in the chimney effect. Extensive research in the field of architecture on the chimney effect, particularly solar chimneys, has provided the theoretical foundation for optimizing applications based on the chimney effect in industrial settings. Zang and Yang [10] used numerical simulations to reveal the concentrated phenomena of flow transition, velocity enhancement, and temperature increase near the walls of solar chimneys, while Yao *et al*. [11] quantified the non-linear effects of the Rayleigh number and aspect ratio on the mass-flow rate of underground solar chimneys, and Gan *et al.* [12] systematically studied buoyancy-driven flow and heat transfer in vertical cavities with different aspect ratios. In terms of structural optimization, Hosien and Selim [13] pointed out that increasing the length of the solar chimney and the air-flow channel gap can enhance performance. Kong *et al*. [14] used CFD to determine the latitude and seasonal dependence of the optimal tilt angle for rooftop solar chimneys. Zhang *et al*. [15] further demonstrated that increasing the chimney height and optimizing the inlet position in multi-room buildings can significantly enhance ventilation efficiency. Regarding environmental factors, Wang *et al.* [16] found that external wind fields can alter the optimal design parameters of solar chimneys but also reduce flow resistance and improve overall performance. In terms of architectural applications, Hao *et al*. [17] pointed out that indoor heat sources and solar radiation can synergistically enhance ventilation. Gu *et al*. [18] proposed and validated a novel rooftop solar chimney combining wind pressure and thermal pressure drive, which demonstrated significant performance improvements. Moosavi *et al*. [19] integrated solar chimneys, wind towers, and sprinkler systems to design a composite ventilation system suitable for arid climates. Addition-

ally, Vargas-Lopez *et al*. [20] conducted transient modelling studies on solar chimneys, incorporating phase-change materials to enhance performance, and proposed a dual-channel model suitable for building energy consumption simulation. Wang *et al.* [21] conducted a multi-dimensional evaluation of Trombe walls based on solar passive heating, including classification systems, experimental methods, modelling techniques, and technical-economic-environmental indicators, thereby advancing the development and application of passive solar technology. Yang *et al*. [22] pointed out that thermal buoyancy can drive natural ventilation in industrial buildings. Villar-Ramos *et al*. [23] developed a single-channel solar chimney with adjustable parameters for humid climates, which can increase ventilation volume in enclosed spaces by five times. Jun *et al*. [24] pointed out that solar chimneys can achieve zero-energy passive ventilation in green buildings, proposing a distributed heating concept. Through innovative design of interlaced heat-absorbing plates, they improved the uniformity of outlet flow velocity. The aforementioned studies have made significant progress in mechanism exploration, parameter optimization, system integration enhancement, and modelling methods, providing a foundation for the design and engineering application of the chimney effect under different usage conditions.

Previous studies mainly optimized cooling bed structures or adjusted process parameters (*e.g.*, reducing moving speed, lowering bed temperature, or extending residence time) to suppress local overcooling of flat steel, but these approaches often reduce production efficiency. To date, the chimney effect has not been introduced into flat steel cooling. As a passive flow regulation mechanism, it can suppress upward air-flow at bed gaps, improve temperature uniformity, and reduce bending without affecting productivity, representing a novel attempt. However, the effects of chimney structural parameters on air-flow and heat transfer remain unclear. Therefore, this study employs numerical simulation design and compare different chimney configurations, with particular attention chimney geometry and cold air inlet positions, in order to evaluate their influence on velocity and temperature fields. The objective is to assess the feasibility of chimney devices for flat steel cooling and to provide theoretical and engineering guidance for reducing bending defects.

Numerical calculation method

Physical model

Figure 1 shows the schematic diagram of the cooling bed structure. Based on the design drawings and production process parameters of the flat steel production-line of a certain steel plant, a physical model of the cooling bed area was constructed. Taking into account the large size of the cooling bed and the periodic arrangement of the straightening plates, a representative local cross-sectional model was established. Flat steel segments are placed on straightening plates and the top of the plates is equipped with a heat insulation cover. There

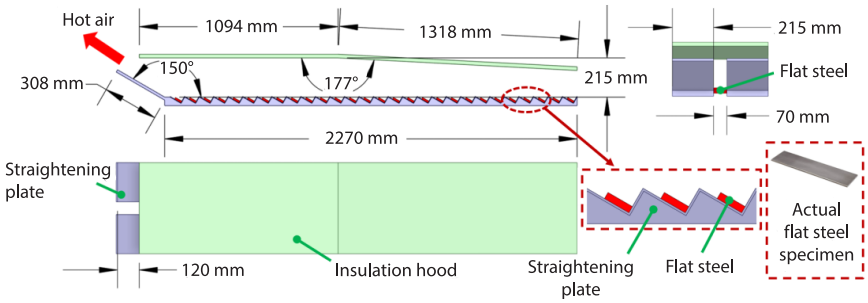

Figure 1. Schematic diagram of the cooling bed structure

are gaps between adjacent plates that facilitate the movement of the flat steel using the rack. During the operation of the rack, the steel moves to the right, that is, towards the cold side of the cooling bed. The hot air is discharged through the gap between the left side of the bed body and the insulation cover.

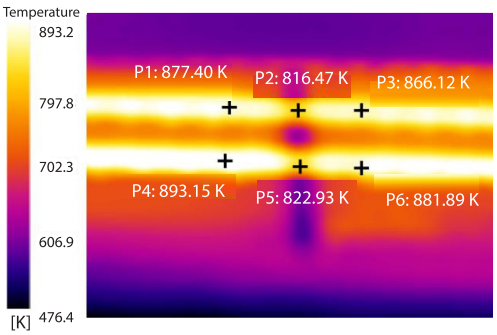

Figure 2. Flat steel infrared image

Figure 2 shows a tested infrared image of flat steel. The temperature of the flat steel at the gaps (P2, P5) is lower than that at non-gap locations (P1, P3, P4, P6). Compared with other areas, the gaps between the straightening plates result in higher air velocities at these gaps, so the steel segments on the gaps cool down faster and have lower temperatures. To reduce the air velocity at the gaps, the wind speed at the cooling bed gaps maybe be lowered through the suction effect of chimney effect structures and mechanical extraction devices.

Chimney effect structures

Three structures of the chimneys were designed: mixing of hot and cold air, small-pipe hot air, large-pipe hot air, as shown in fig. 3. In the mixing of hot and cold air, hot air from the cooling bed enters the mixing chimney through the hot air inlet and combines with the cold air extracted from the cold air inlet beneath the cooling bed, before being discharged through the mixing air out. In the separation structures, two concentric ducts of different diameters are used. In small-pipe hot air, hot air from the cooling bed enters the small pipe through the hot air inlet. Inside, the hot air exchanges heat with the cold air in the large pipe, heating it, lowering its density, and causing upward flow that drives the cold air inlet beneath the cooling bed to extract cold air. The hot air in the small pipe is then discharged through the hot air outlet, while the cold air in the large pipe, after being heated, exits through the cold air outlet. In large-pipe hot air, hot air from the cooling bed enters the large pipe via the hot air inlet and heats the air within the small pipe. The heated air rises, creating a suction effect that drives the cold air inlet beneath the cooling bed to extract cold air. Ultimately, the hot air in the large pipe is discharged through the hot air outlet, while the air in the small pipe, after being heated, exits through the cold air outlet.

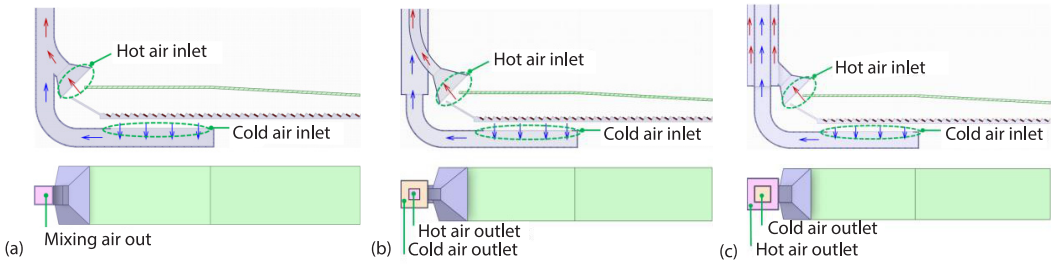

Figure 3. Chimney effect structures; (a) mixing of hot and cold air, (b) small-pipe hot air, and (c) large-pipe hot air

Mechanical air intake structure

Figure 4 shows the mechanical air intake structure. Mechanical ventilation equipment consists of a fan and suction ducts. It consumes electrical energy and uses the pressure differ-

ence created by the fan to drive the suction ducts, thereby reducing the wind speed at the gaps. Figure 5 illustrates the distance between the air intake and the cooling bed. The distance, H, between the intake and the cooling bed is adjusted to determine the optimal spacing for reducing gap air-flow velocity.

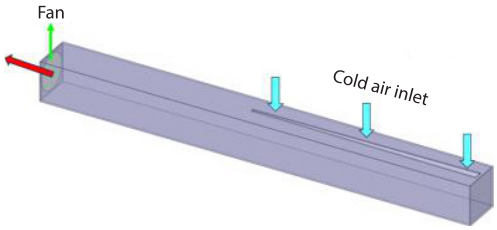

Figure 4. Mechanical air intake structure

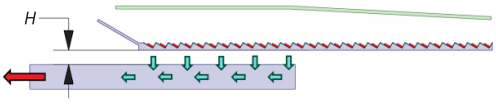

Figure 5. The distance between the air intake and the cooling bed

Figure 6 shows the air intake structures. To achieve uniform air velocity at the gaps corresponding to different positions of flat steel beneath the cooling bed. By adjusting the θ of air intake structures the wind speed at the air inlet is kept consistent. Air intake structure was simulated individually, with monitoring lines placed at the intake inlets to record air-flow velocity. To evaluate the effectiveness of the chimney-effect structures and the mechanical exhaust system, an initial state of the cooling bed without any extraction device was conducted. The air-flow velocities at the gap locations for each structure were then compared initial state. Figure 7 shows the numbering of the gaps. To obtain accurate air-flow velocity at each gap, monitoring surfaces were created at the first 11 gaps. The area-weighted average velocity across each surface was calculated and numbered sequentially from the hot air side. Meanwhile, the temperature difference, ΔT, of each flat steel between the gap and non-gap positions was recorded, and the ΔT values were sequentially numbered from the hot air outlet to the inlet.

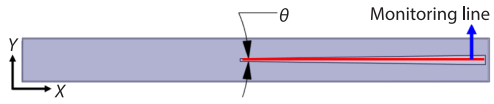

Figure 6. Air intake structure

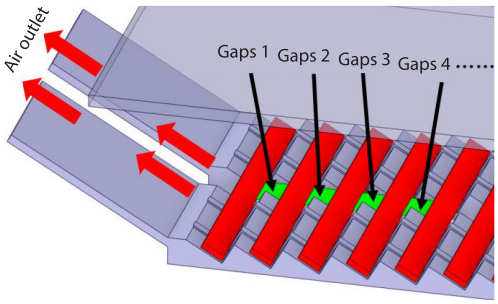

Figure 7. Gap numbering

Governing equations

To simplify the calculations and ensure the reliability of the results, the following assumptions were made for the physical model when establishing the mathematical model of the cooling bed:

- The air as Newtonian fluid, and at high temperatures, the stress-shear rate relationship is essentially linear, making it a typical Newtonian fluid.
- Assuming that the air density is a function of temperature, capture buoyancy-driven phenomena caused by temperature gradients, accurately reflecting natural-convection characteristics.
- Air-flow meets no slip boundary condition, with zero velocity on the flat steel surface and cooling bed surface, consistent with boundary-layer theory at the macroscopic scale.

– The air-flow is steady-state. Although flat steel cooling is a time-dependent process, in the cooling bed, the flat steel moves forward at fixed time intervals, and at each moment there is a typical temperature distribution pattern on the cooling bed, giving the system a certain degree of periodicity and quasi-steady-state characteristics. Meanwhile, air is a low thermal inertia fluid that can respond quickly to changes in boundary conditions, so the air-flow field can be regarded as steady-state.
– Ignoring the thermal radiation effects within the fluid, although the surface temperature of the flat steel is relatively high, the radiation capacity of the air itself is relatively weak. Therefore, the thermal radiation effects in the air are not considered, and only the surface radiation between the flat steels and between the flat steels and the environment is considered.

The basic governing equations of the model are based on the laws of conservation of mass, momentum, and energy.

Mass conservation equation:

$$\nabla(\rho u) = 0 \tag{1}$$

where ρ [kgm^{-3}] is the fluid density and u [ms^{-1}] – is the velocity vector.

Momentum conservation equation:

$$\rho(u\nabla u) = -\nabla p + \nabla\boldsymbol{\tau} + \rho g + F \tag{2}$$

where p [Pa] is the pressure, $\boldsymbol{\tau}$ [Pa] – the viscous stress tensor, g [ms^{-2}] – the gravitational acceleration, F [Nm^{-3}] – the other volumetric forces.

Realizable k-ε:

$$\rho u_i \frac{\partial(k)}{\partial x_j} = \frac{\partial}{\partial x_j}\left[\left(\mu + \frac{\mu_i}{\sigma_k}\right)\frac{\partial k}{\partial x_j}\right] + P_k - \rho\varepsilon \tag{3}$$

$$\rho u_i \frac{\partial(\varepsilon)}{\partial x_i} = \frac{\partial}{\partial x_i}\left[\left(\mu + \frac{\mu_i}{\sigma_k}\right)\frac{\partial \varepsilon}{\partial x_j}\right] + \rho C_1 S\varepsilon - \rho C_2 \frac{\varepsilon^2}{k + \sqrt{v\varepsilon}} \tag{4}$$

where u_i [ms^{-1}] is the velocity component, x_i – the co-ordinate component in the i-direction, k [m^{2}s^{-2}] – the turbulent kinetic energy, ε [m^{2}s^{-2}] – the turbulent dissipation rate, μ and μ_i [Pa·s] – the molecular viscosity and turbulent viscosity, respectively, P_k [kgm^{-1}s^{-3}] – the generating term, S [s^{-1}] – the strain rate tensor modulus, ν [m^{2}s^{-1}] – the kinematic viscosity, and C_1 and C_2 – the model constant.

Gas density model:

$$\rho = \frac{P}{\mathrm{R}TZ} \tag{5}$$

where P [Pa] – is the pressure of the gas, T [K] – the absolute temperature of the gas, R [Jmol^{-1}K^{-1}] – the gas constant, and Z – the compression factor of the gas.

Surface to surface model:

$$q_i = \varepsilon_i \sigma T_i^4 - \sum_{j=1}^{N} F_{ij}\varepsilon_j \sigma T_j^4 \tag{6}$$

where q_i [Wm^2] is the net radiative heat flux from surface, ε_i [Wm^{-2}K^{-4}] – the surface emissivity, σ – the Stefan-Boltzmann constant, T_i [K] – the surface temperature, and F_{ij} – the view factor.

Boundary conditions and solution

The geometric model is created using SpaceClaim software, and the divided polyhedron mesh is imported into the solver. The air density was modeled using the real-gas-nist

equation of state. The realizable k-ε turbulence model was adopted, and radiation effects were handled using the surface-to-surface (S2S) radiation model.

For pressure-velocity coupling, the Coupled algorithm was selected. Pressure discretization used the body force weighted scheme, while momentum equations, turbulent kinetic energy, and turbulent dissipation rate equations were discretized using the second-order upwind scheme.

Figure 8 shows the cooling bed model and the computational domain. Calculate the dimensions of the area: length 4205 mm, width 500 mm, and height 2095 mm.

The upper boundary condition of the cooling bed is pressure-outlet, the wall boundary of the cooling bed is an adiabatic boundary condition, the front and rear boundary conditions of the cooling bed are adiabatic boundary conditions, the velocity-inlet is the actual measured value of 0.05 m/s, the inlet temperature is the actual measured value of 303.15 K, and the boundary condition of the flat steel is a heat flux boundary condition.

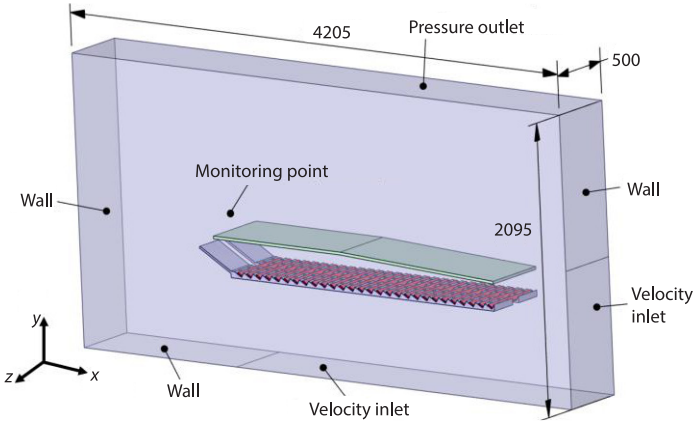

Figure 8. Cooling bed model and calculation area

Grid independence check and verification

To balance computational accuracy and efficiency, grid independence verification was conducted by dividing the grid into five sets with different numbers of cells, ensuring that the selected grid can both guarantee the accuracy of the results and reduce the computational load.

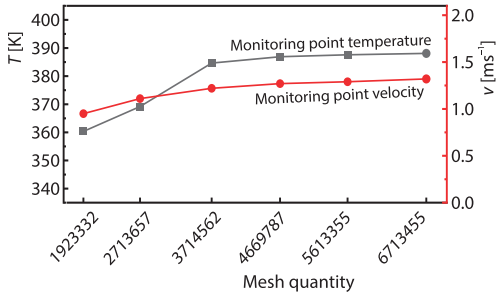

Figure 9. Grid independence verification

The results of the grid independence study are shown in fig. 9. When the number of grids exceeds 3714562, the differences in temperature and wind speed at the monitoring points are small, with variations of approximately 2%, which can be neglected. Therefore, 3714562 grids were adopted in the simulation.

Verification of the model

Table 1 presents the comparison between the simulated data and the experimental data. The accuracy of the cooling bed model was verified through our own experimental measurements. The comparison of the simulated data and the experimental data at the monitoring

points in fig. 8 shows that the error is relatively small. This indicates that the model has high reliability.

Table 1. Comparison of experimental results with simulation results

Parameters	Simulation result	Experimental result	Relative error [%]
Temperature [K]	433.36	448.15	3.3
Velocity [ms^{-1}]	1.86	2.01	7.46

Results and discussion

Analysis of air intake structures

Figure 10(a) shows the velocity distribution at the intake openings of one air inlet. As θ increases, the overall velocity decreases because a larger θ increases the intake resistance and induces flow separation near the inlet. This intensifies the pressure gradient, causes energy loss, and ultimately reduces the suction velocity. For most angles, the velocity significantly drops with increasing distance, X, and this trend becomes more pronounced at larger angles. Figure 10(b) shows velocity variance across the entire intake. With increasing θ, the velocity variance increases, mainly due to the enhancement of turbulence intensity, which deteriorates the uniformity of the flow field. Under small-angle conditions (*e.g.*, $\theta = 0°$ and 0.5°), not only is the suction velocity higher, but the fluctuations are smaller, leading to a more stable flow field. In contrast, at larger angles, the wind speed decreases significantly and fluctuations intensify, leading to poorer suction performance and reduced velocity uniformity. Therefore, $\theta = 0.5°$ provides the optimal condition, as they maintain high suction velocity while minimizing fluctuations.

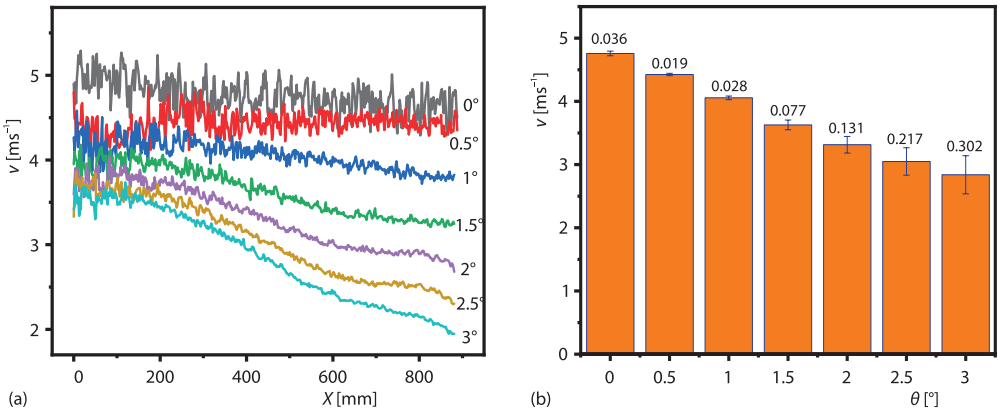

Figure 10. Air intake structure velocity and velocity variance diagram; (a) air intake structure velocity and (b) air intake structure velocity variance

In the design of cold air inlet, reducing the angle helps to achieve higher and more stable air-flow. Conversely, increasing the angle will result in a decrease in speed and a significant increase in air-flow volatility. Therefore, air intake structure with $\theta = 0.5°$ was selected for further analysis. This intake structure was driven by two different methods: a 15 W fan and chimney-effect-induced natural-convection.

Simulation analysis of chimney effect structures

Figure 11 shows the velocity vector in the air-flow field for the three chimney-effect structures. In mixing of hot and cold air structure, the upward motion of hot air in the upper pipe generates a buoyancy-driven effect, which entrains cooler air from the lower pipe and thereby enhances the overall buoyancy effect. In the small-pipe hot air and large-pipe hot air structures, heat transfer from the hot air reduces the density of the air inside the cooler pipe, causing it to rise. This buoyancy-induced suction effect is strongly influenced by the temperature of the hot air pipe, with higher temperatures producing stronger upward driving forces.

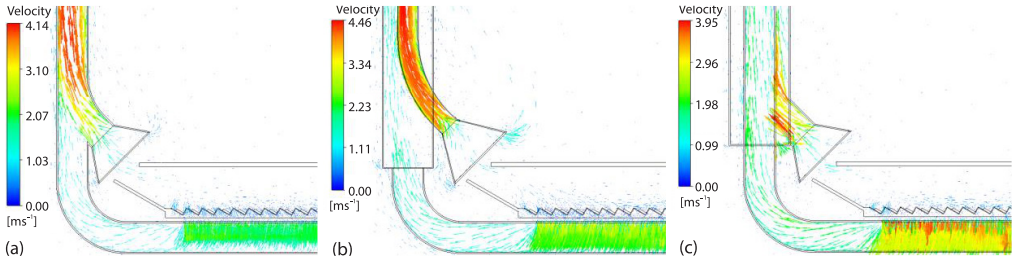

Figure 11. Air velocity vector diagram in chimneys; (a) mixing of hot and cold air, (b) small-pipe hot air, and (c) large-pipe hot air

Figure 12 shows the velocity cloud diagram of the chimney effect structure. The results indicate that structural differences have a significant impact on the velocity field. In the hot–cold mixing and small-pipe hot air structures, the hot air channels remain relatively unobstructed, and the buoyancy-driven acceleration effect is enhanced, resulting in significantly higher air-flow velocities compared with the large-pipe hot air structure. In contrast, in the large-pipe hot air structure, the inflow of hot air is impeded, thereby leading to a noticeable reduction in air-flow velocity. Figure 13 shows the temperature cloud diagram of the chim-

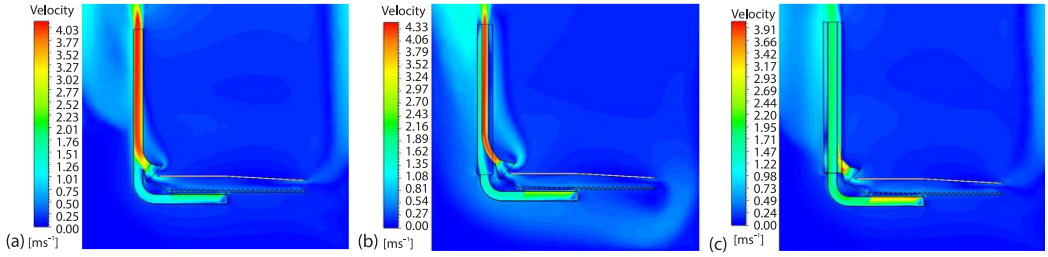

Figure 12. Air velocity diagram in chimneys; (a) mixing of hot and cold air, (b) small-pipe hot air, and (c) large-pipe hot air

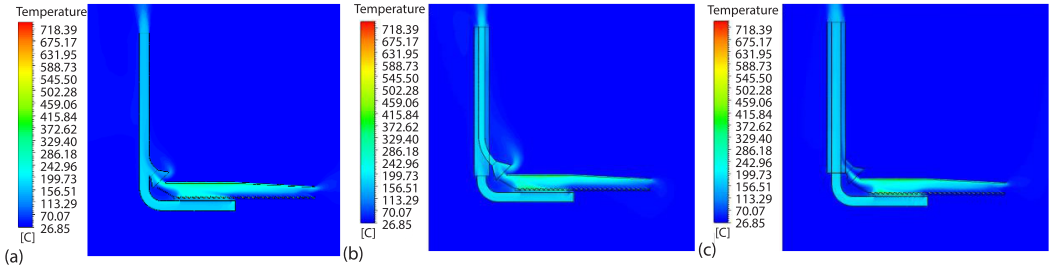

Figure 13. Temperature diagram in chimneys; (a) mixing of hot and cold air, (b) small-pipe hot air, and (c) large-pipe hot air

ney effect structure. In the large tube of the small-pipe hot air structure and the small tube of the large-pipe hot air structure, high temperature air accumulates, forming stable thermal regions. The accumulated hot air markedly decreases density and consequently enhances buoyancy-driven capability. Figure 14 shows the pressure distributions of the three chimney-effect structures. The results indicate that in the mixing of hot and cold structure, hot air entering from the hot air inlet generates a pressure difference that induces the motion of cold air in the lower pipe. Because the mixed air is quickly discharged, the internal temperature is lower than in the other two structures, resulting in relatively weaker negative pressure. In contrast, in the small-pipe and large-pipe hot air structures, the accumulation of high temperature air establishes a pronounced longitudinal pressure drop, and the negative pressure region expands as the temperature difference increases. This negative pressure serves as the primary driving force of the exhaust system. Therefore, optimizing structural configuration strengthen temperature-driven buoyancy is essential for enhancing the performance of the chimney effect.

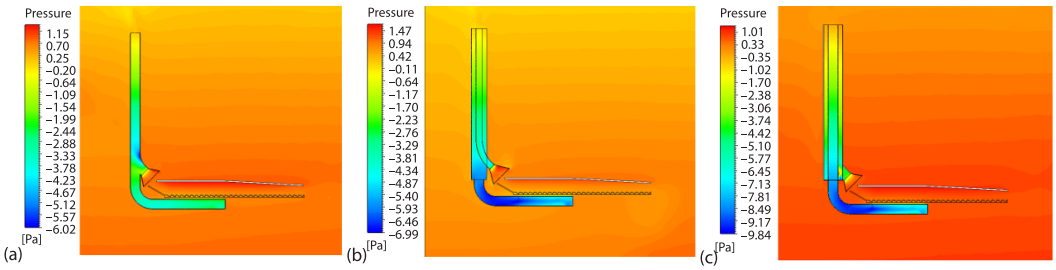

Figure 14. Pressure diagram in chimneys; (a) mixing of hot and cold air, (b) small-pipe hot air, and (c) large-pipe hot air

Figure 15(a) shows the air-flow velocity in the cooling bed gap and the ΔT between the flat steel at the gap and non-gap locations for the hot and cold air mixing structure. The air velocity at the gap gradually increases and ΔT increases with the increase of H. When H = 20 mm, the wind speed at the gap is the lowest. As H increases, the temperature of the air drawn in by the cold air inlet decreases. Since the cold and hot air in this structure are discharged together after mixing, the temperature of the discharged mixing air outlet gradually decreases, the chimney effect weakens, and thus the air-flow rate at the cold air inlet decreases, as shown in fig. 15(b), the wind speed at the gap gradually increases.

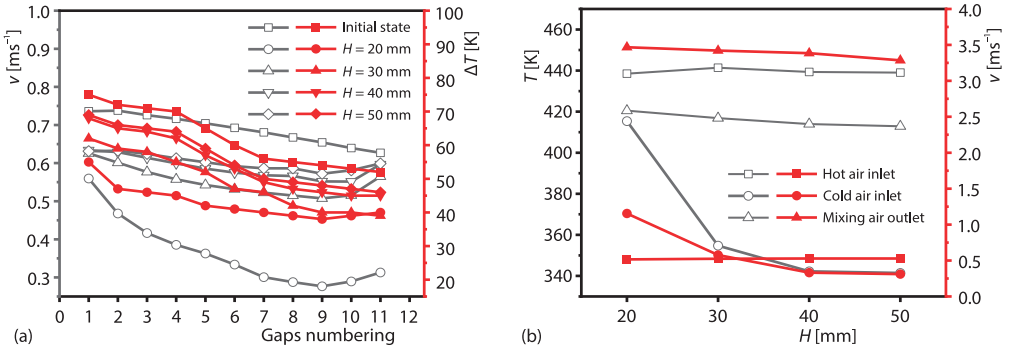

Figure 15. Mixing of hot and cold air structure; (a) air-flow velocity and ΔT at the gap and (b) temperature and mass-flow at air inlet and outlet

Figures 16(a) and 17(a) show the air-flow velocity and the ΔT between the flat steel at the gap and non-gap locations for the cooling bed gaps of the small-pipe hot-air structure and the large-pipe hot-air structure. The air velocity at the gap gradually increases and ΔT increases as H increases. When $H = 20$ mm, the air velocity at the gap is minimized and ΔT is minimized. However, for large-pipe hot air structure, when $H = 30$ mm, the wind speed at the gap is lower than theirs. As shown in figs. 16(b) and 17(b), in these two structures, the increase of H leads to a decrease in the temperature of the air sucked in by the cold air inlet, thereby reducing the temperature of the cold air outlet and weakening the chimney effect. This causes the air-flow velocity of the cold air inlet and the cold air outlet to decrease, and as a result, the wind speed at the gap gradually increases. Small-pipe hot air structure uses the hot air in the small pipe to heat the cold air in the large pipe, and large-pipe hot air structure uses the hot air in the large pipe to heat the cold air in the small pipe. Moreover, the flow channels of the cold and hot air in the two structures are separate. Therefore, when the temperature of the air sucked in by the cold air inlet is too high, It will lead to a decrease in the air temperature entering the hot air inlet. The wind speed of the hot air inlet and the hot air outlet hardly changes significantly with the increase of H. When $H > 20$ mm, the buoyancy of the gas in the cold pipe is mainly provided by the hot air pipe. However, when $H = 2\ 0$ mm, the cold air inlet sucks in high temperature air. At this time, the buoyancy in the cold pipe is mainly provided by the high temperature air sucked in by the cold air inlet. This is because the temperature of the sucked high temperature air is much higher

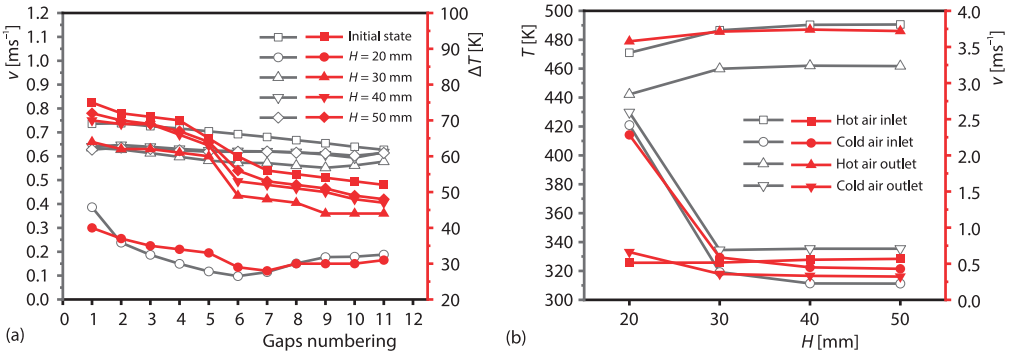

Figure 16. Small-pipe hot air structure; (a) air-flow velocity and ΔT at the gap and (b) temperature and mass-flow at air inlet and outlet

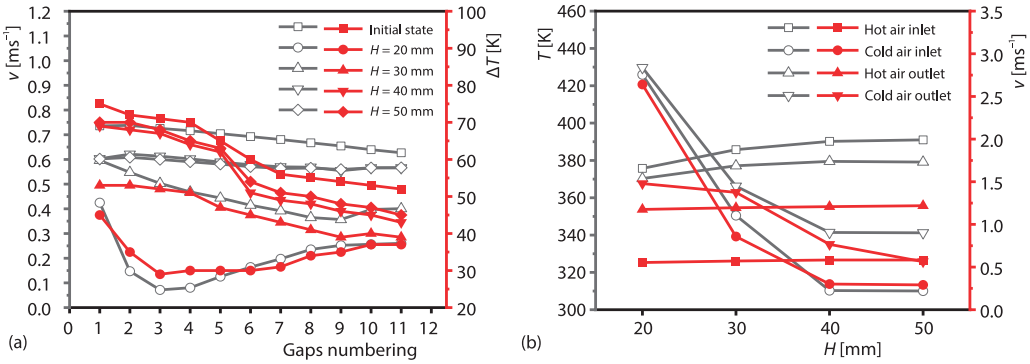

Figure 17. Large-pipe hot air structure; (a) air-flow velocity and ΔT at the gap and (b) temperature and mass-flow at air inlet and outlet

than that of the cold air heated by the hot air pipe. At this time, the chimney effect is strong. The wind speed at the cold air inlet is high, which can effectively reduce the wind speed at the gap. Among these two structures, as H increases, the main buoyancy source driving the structure changes from the hot air pipe to the high temperature air sucked in by the cold air inlet. Moreover, when the main buoyancy source is the high temperature air sucked in by the cold air inlet, the chimney effect is strong and can effectively reduce the air-flow velocity at the gap.

Simulation analysis of mechanical air intake structure

Figure 18 shows the air-flow velocity at the gap between the mechanical exhaust equipment and the ΔT between the flat steel at the gap and non-gap locations. As H increases, the wind speed at the gap decreases first and then increases, and ΔT also decreases first and then increases. When H is 20 mm, the wind speed at the gap cannot be effectively reduced. This is because the negative pressure generated by the fan is too strong, causing the wind speed at the suction port to be very high and all the hot air at the gap to be sucked away. When the distance H between the suction port and the straightening plate of the mechanical air intake structure is 30 mm to 50 mm, the air-flow velocity at the gap can be well reduced. At this time, when observed in the sequence of numbers, the air-flow velocity at the gap gradually increases.

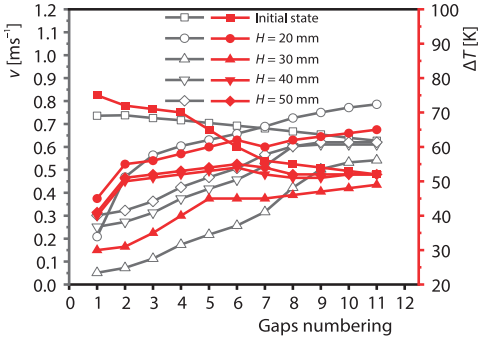

Figure 18. Air-flow velocity and ΔT at the gap of the mechanical exhaust equipment

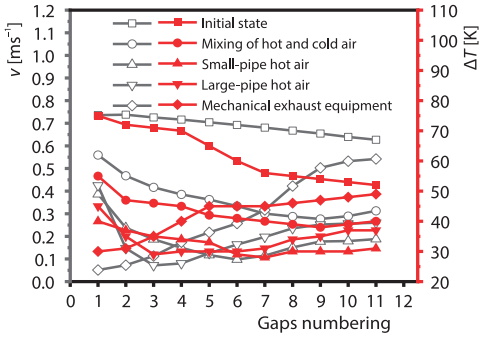

Figure 19. Minimum air-flow velocity and ΔT at the gap of the four structures

Unlike the chimney effect structure which relies on the buoyancy effect of hot air, the mechanical air intake structure utilizes the negative pressure generated by the fan. Although the suction port will also draw in high temperature gas, the mechanical exhaust equipment is a horizontal device. The high temperature gas will be horizontally discharged by the fan and will not produce the chimney effect. The negative pressure generated by high temperature air is lower than that produced by the fan. So as H increases, the trend of wind speed variation at the gaps of the mechanical air intake structure is different from that of the chimney effect structure.

Figure 19 shows the minimum air-flow rate at the four structural gaps and the ΔT between the flat steel at the gap and non-gap locations. When H is set to an appropriate value, all schemes can reduce the wind speed at the gap. Among them, small-pipe hot air structure, large-pipe hot air structure, and mechanical air intake structure have a better speed reduction effect than the mixing of hot and cold air structure. The mixing of hot and cold air structure can reduce the air velocity at the gap by 47.32%, while small-pipe hot air structure and large-pipe hot air structure reduce it by 73.8% and 70.79%, mechanical air intake structure can reduce the air velocity at the gap by 57.78%. Regarding the ΔT of the steel bars between slit and non-slit positions, the mixed hot–cold air structure reduces ΔT by 30.89%, while the small-tube and large-tube hot air structures achieve reductions of 47.73% and 45.38%,

respectively, and the mechanical air-supply structure reduces ΔT by 45.39%. Overall, the small-tube hot air configuration demonstrates the best performance in both reducing air-flow velocity and minimizing ΔT, and can thus be considered the optimal structure among the four schemes.

Conclusions

To address the problem of localized rapid cooling of flat steel during the cooling bed process, four different types of suction devices were designed to reduce the cooling rate of flat steel at the cooling bed gaps. The computational fluid dynamics method was employed to simulate the flow fields of four different suction devices during the cooling process of the flat steel bed. The factors influencing the air velocity in the gap of the cooling bed were analyzed, and the conclusions are as follows.

- The results indicate that the air-flow velocity at the cooling bed gaps directly affects ΔT between gap and non-gap positions of flat steel, with higher velocities leading to larger ΔT. All four proposed structures effectively reduced both air-flow velocity and ΔT, among which the small-pipe hot air structure performed best (73.8% reduction in air-flow velocity and 47.73% reduction in ΔT) and can be considered the optimal solution.
- In terms of energy efficiency, small pipe hot air structure outperforms the other three designs. Unlike the mechanical suction device, this configuration requires no electrical energy and utilizes waste heat to generate a natural chimney effect, thereby providing advantages in both energy conservation and environmental sustainability.

Acknowledgment

This work was supported by Key R&D Plan of Shandong Province (Grant No. 2022CXGC020901) and Young Talent of Lifting Engineering for Science and Technology in Shandong, China (Grant No. SDAST2024QTA048).

Nomenclature

F – other body forces, [Nm^{-3}]
F_{ij} – view factor
g – gravitational acceleration, [ms^{-2}]
p – pressure, [Pa]
q_i – net radiative heat flux from surface i, [Wm^{-2}]
R – gas constant, [Jmol^{-1}K^{-1}]
S – modulus of the strain rate tensor, [s^{-1}]
T – absolute temperature, [K]
T_i – surface temperature, [K]
u_i – velocity component, [ms^{-1}]
v – velocity vector, [ms^{-1}]
x_i – co-ordinate component in the i direction, [m]
Z – compressibility factor

Greek letters

μ – molecular viscosity, [Pa·s]
μ_t – turbulent viscosity, [Pa·s]
ρ – density, [kgm^{-3}]
σ – Stefan-Boltzmann constant, [Wm^{-1}K^{-4}]
τ – viscous stress tensor [Pa]
ε – turbulent dissipation rate, [m^{2}s^{-2}]
ε_i – surface emissivity

Subscript

i – co-ordinate component
j – co-ordinate component

References

[1] Xing, H., Production Process and Application of Hot-Rolled Flat Steel (in Chinese), *Metallurgy and Materials*, *44* (2024), 1, pp. 91-93
[2] An, H. N., *et al*., A Model for Deformation, Temperature and Phase Transformation Behavior of Steels on Run-Out Table in Hot Strip Mill, *Journal of Materials Processing Technology*, *128* (2002), 1-3, pp. 216-225
[3] Qiu, Z., *et al*., Numerical Simulation of Transverse Bending of Hot Rolled Medium Carbon Steel Strip (in Chinese), *Iron and Steel*, *52* (2017), 5, pp. 61-65, 93
[4] Li, J., *et al*., Finite Element Analysis of Bending Deformation during Cooling Process of Hot-Rolled L-Shaped Steel Based on Secondary Development of ABAQUS (in Chinese), *Journal of Iron and Steel Research*, *34* (2022), 12, pp. 1408-1416

[5] Chen, L., *et al*., Effects of Cooling on Bending Process of Heavy Rail Steel After Hot Rolling. Metallography, *Microstructure, and Analysis*, *5* (2016), 3, pp. 196-206
[6] Pernia, A., *et al*., Realistic Modelling and Optimisation of Steel Section Cooling Process, Ironmaking & Steelmaking, *38* (2011), 1, pp. 17-27
[7] Ren, B., *et al*., Research on Reducing Bending Problems of Cold Heading Alloy Steel (in Chinese), *Metallurgical Collections*, *5* (2014), pp. 22-24
[8] Kong, L., *et al*., Bending Control Analysis of CM435 Hot Rolling Billet (in Chinese), *Hebei Metallurcy*, *3* (2018), pp. 31-33
[9] Cai, Z., Song, G., Bending Control with Cooling Bed Technology for Alloy Cold Heading Steel Billet (in Chinese), *Bao-Steel Technology*, *6* (2007), pp. 10-13
[10] Zhang ,T., Yang, H., Flow and Heat Transfer Characteristics of Natural-Convection in Vertical Air Channels of Double-Skin Solar Façades, *Applied Energy*, *242* (2019), May, pp. 107-120
[11] Yao, L., *et al*., Study on Characteristics of Natural Ventilation Strengthened by Solar Chimney in Underground Space (in Chinese), Acta Energiae Solaris Sinica, *42* (2021), 6, pp. 184-190
[12] Gan, G., A parametric Study of Trombe Walls For Passive Cooling of Buildings, *Energy and Buildings*, *27* (1998), 1, pp. 37-43
[13] Hosien, M. A., Selim, S. M., Effects of the Geometrical and Operational Parameters and Alternative Outer Cover Materials on the Performance of Solar Chimney Used for Natural Ventilation, *Energy and Buildings*, *138* (2017), Mar., pp. 355-367
[14] Kong, J., *et al*., A CFD Based Approach for Determining the Optimum Inclination Angle of a Roof-Top Solar Chimney for Building Ventilation, *Solar Energy*, *198* (2020), Mar., pp. 555-569
[15] Zhang, H., *et al*., A Wall Solar Chimney to Ventilate Multi-Zone Buildings, *Sustainable Energy Technologies and Assessments*, *47* (2021), 101381
[16] Wang, Q., *et al*., External Wind on the Optimum Designing Parameters of a Wall Solar Chimney in Building, *Sustainable Energy Technologies and Assessments*, *42* (2020), 100842
[17] Hao, Y., *et al*., Research on the Performance of the Coupling Effect of Indoor Thermal Plume and Solar Chimney Effect, *Renewable Energy Resources*, *40* (2022), 6, pp. 767-772
[18] Gu, Y.,, *et al*., Numerical Investigation on Ventilation Performance of a New Roof Solar Chimney, *Journal of Engineering for Thermal Energy and Power*, *31* (2016), 6, pp. 99-104
[19] Moosavi, L., *et al*., New Design for Solar Chimney With Integrated Windcatcher for Space Cooling and Ventilation, *Building and Environment*, *181* (2020), 106785
[20] Vargas-Lopez, R., *et al*., Mathematical Models of Solar Chimneys with a Phase Change Material for Ventilation of Buildings: A Review Using Global Energy Balance, *Energy*, *170* (2019), Mar., pp. 683-708
[21] Wang, D., *et al.*, Classification, Experimental Assessment, Modelling Methods and Evaluation Metrics of Trombe Walls, *Renewable and Sustainable Energy Reviews*, *124* (2020), 109772
[22] Yang, C., *et al.*, Interaction of the Thermal Plumes Generated from Two Heat Sources of Equal Strength in a Naturally Ventilated Space, *Journal of Wind Engineering and Industrial Aerodynamic*s, *198* (2020), 104085
[23] Villar-Ramos, M. M., *et al.*, *et al*., Parametric Analysis of the Thermal Behavior of A Single-Channel Solar Chimney, *Solar Energy*, *209* (2020), Oct., pp. 602-617
[24] Jun, G., *et al*., A Novel Staggered Split Absorber Design for Enhanced Solar Chimney Performance, *Building and Environment*, *224* (2022), 109569

Paper submitted: July 11, 2025
Paper revised: October 13, 2025
Paper accepted: October 14, 2025

2026 Published by the Vinča Institute of Nuclear Sciences, Belgrade, Serbia.
This is an open access article distributed under the CC BY-NC-ND 4.0 terms and conditions.